

Signature of the coexistence of ferromagnetism and superconductivity at KTaO_3 heterointerfaces

Zhongfeng Ning,¹ Jiahui Qian,¹ Yixin Liu,^{2,3} Fan Chen,^{2,3} Mingzhu Zhang,^{2,3} Liwei Deng,^{2,3} Xinli Yuan,⁴ Qingqin Ge,⁴ Hua Jin,² Guanqun Zhang,¹ Wei Peng,^{2,3} Shan Qiao,^{2,3,*} Gang Mu,^{2,3,†} Yan Chen,^{1,‡} and Wei Li^{1,§}

¹*State Key Laboratory of Surface Physics and Department of Physics, Fudan University, Shanghai 200433, China*

²*National Key Laboratory of Materials for Integrated Circuits,
Shanghai Institute of Microsystem and Information Technology,
Chinese Academy of Sciences, Shanghai 200050, China*

³*University of Chinese Academy of Sciences, Beijing 100049, China*

⁴*Thermo Fisher Scientific China, Shanghai 201203, China*

(Dated: November 28, 2023)

The coexistence of superconductivity and ferromagnetism is a long-standing issue in the realm of unconventional superconductivity due to the antagonistic nature of these two ordered states. Experimentally identifying and characterizing novel heterointerface superconductors that coexist with magnetism is challenging. Here, we report the experimental observation of long-range ferromagnetic order at the verge of two-dimensional superconductivity at KTaO_3 heterointerfaces. Remarkably, we observe in-plane magnetization hysteresis loop persisting to above room temperature with direct current superconducting quantum interference device measurements. Furthermore, both the first-principles calculations and the x-ray magnetic circular dichroism measurements reveal that the observed robust ferromagnetism is attributed to the presence of oxygen vacancies that localize electrons in nearby Ta $5d$ states. Our findings not only indicate KTaO_3 heterointerfaces as unconventional superconductors with time-reversal symmetry breaking, but also inject a new momentum to the study of the delicate interplay between superconductivity and magnetism boosted by strong spin-orbit coupling inherent to the heavy Ta in $5d$ orbitals of KTaO_3 heterointerfaces.

Introduction

Oxide heterointerfaces exhibit a wide range of emergent quantum phenomena inaccessible in their bulk individuals due to the strong interplay between electrons with Coulomb interaction and the interfacial electron-phonon coupling at the interface^{1–3}. Among them, a landmark oxide interface is $\text{LaAlO}_3/\text{SrTiO}_3$ ⁴, which displays a plethora of appealing physical properties, including two-dimensional electron gases with high electron mobility⁵, strong Rashba-like spin-orbit coupling^{6–8}, interfacial superconductivity^{9,10}, and ferromagnetism^{11,12}. In particular, the coexistence of superconductivity and ferromagnetism has also been unveiled by high-resolution magnetic torque magnetometry¹³, scanning superconducting quantum interference device (SQUID)¹⁴, and magnetoresistance¹⁵. This suggests the presence of an unconventional and nontrivial superconducting phase in the ground state, such as an intriguing Fulde-Ferrell-Larkin-Ovchinnikov-type condensate of Cooper pairs with finite momentum¹⁶ and a mixed-parity superconducting phase with an admixture of spin-singlet and spin-triplet pairing components¹⁷. However, the extremely low superconducting critical temperature T_c (below 250 mK) of SrTiO_3 heterointerfaces makes it challenging to experimentally investigate its properties^{9,18,19}, leading to that the origin of these quantum phases has remained so far elusive^{20–22}.

Very recently, an unexpected crystalline-orientation-dependent superconductivity has been observed at KTaO_3 heterointerfaces with T_c of 2 K^{23,24}. This is nearly two orders of magnitude higher in T_c than its three-dimensional counterpart²⁵. The experimental find-

ings also suggest that the electronic states near the Fermi level derived from Ta $5d$ orbitals with strong spin-orbit coupling play a decisive role in electronic conduction at the KTaO_3 heterointerfaces^{26–29}. Furthermore, the existence of intrinsic anomalous Hall effect has been observed by electrical transport measurements at non-superconducting KTaO_3 heterointerfaces³⁰, and this indicates an emergent ferromagnetism with time-reversal symmetry breaking. In addition, at superconducting KTaO_3 heterointerfaces, the in-plane azimuthal angle-dependent magnetoresistance and the superconducting critical field exhibit striking twofold symmetric oscillations deep inside the superconducting phase, whereas the anisotropy vanishes in the normal phase, in our recent prominent study³¹. This suggests an intrinsic nature of the mixed-parity unconventional superconducting ground state with an admixture of s -wave and p -wave pairing components inherent to the inversion symmetry breaking at the KTaO_3 heterointerfaces³¹. Although the component of p -wave pairing could be stabilized by the long-range ferromagnetic order^{32–34}, the existence of ferromagnetism at superconducting KTaO_3 heterointerfaces, similar to that observed at superconducting SrTiO_3 heterointerfaces, has yet to be addressed experimentally.

Here, using the measurements of direct current SQUID, we observe a conspicuous signal of in-plane ferromagnetic hysteresis loop at the verge of two-dimensional superconductivity at the KTaO_3 heterointerfaces, assigning to an intrinsic ferromagnetism that persists to above room temperature. Moreover, by first-principles calculations and x-ray magnetic circular dichroism (XMCD)

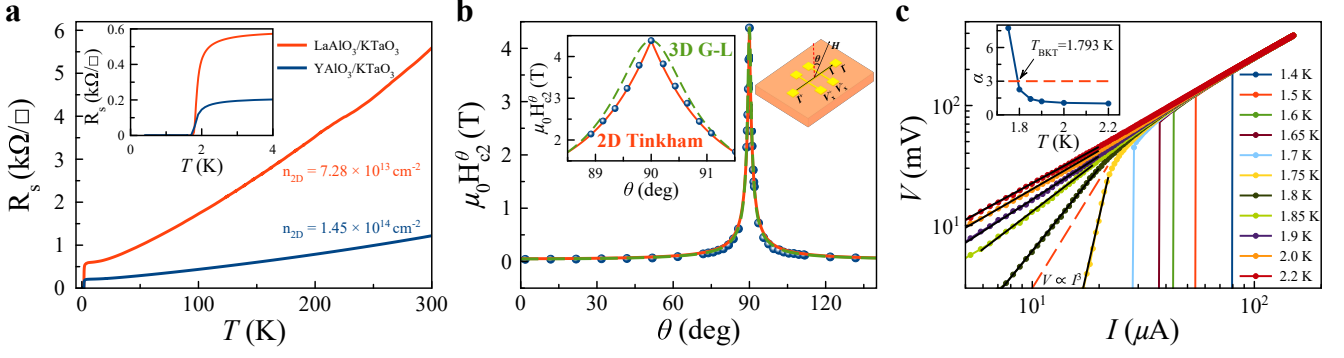


FIG. 1. **Two-dimensional superconductivity of KTaO₃ heterointerfaces.** **a** Longitudinal electrical resistance R_s as a function of temperature for LaAlO₃ and YAlO₃ films grown on the KTaO₃(111) substrates. Inset: magnified view of the low temperature regime. **b** Out-of-plane polar angular θ dependence of the upper critical field $\mu_0 H_{c2}^\theta$ for LaAlO₃/KTaO₃(111). Inset: magnified view of the regime around $\theta = 90^\circ$. The red solid and green dotted lines are theoretical fits using the two-dimensional (2D) Tinkham and the three-dimensional (3D) anisotropic Ginzburg-Landau (G-L) models, respectively. **c** I - V measurements at various temperatures on logarithmic scale for LaAlO₃/KTaO₃(111). The red dashed line denotes $V \propto I^\alpha$. Inset: the extracted power-law fitting exponent α as a function of the temperature T . The BKT transition temperature $T_{\text{BKT}} = 1.793$ K is defined by $\alpha = 3$.

measurements, we provide an additional evidence for the robust ferromagnetism of KTaO₃ heterointerfaces as due to the local moments of the Ta⁴⁺: 5d¹ ions brought about by the oxygen vacancies that host the two-dimensional electron gases formed at the KTaO₃ heterointerfaces. Notably, these results indicate that KTaO₃ heterointerfaces are time-reversal symmetry breaking superconductors, which offer innovative perspectives on the understanding of the underlying rich superconducting properties at the KTaO₃ heterointerfaces.

Results

Both the LaAlO₃ and YAlO₃ thin films are grown by pulsed laser deposition (PLD) on top of the 5×5×0.5 mm³ single-crystalline KTaO₃(111) substrates (see Methods and our previous study³¹). Atomic force microscopy (AFM) characterization shows that the surface of KTaO₃ substrates and thin films are atomically flat (see Supplementary Fig. 1, YAlO₃ shown in Ref.³¹), suggesting a high-quality growth of the thin films on KTaO₃. On the other hand, x-ray diffraction (XRD) reveals the absence of epitaxial Bragg reflection peaks from both the LaAlO₃ and YAlO₃ thin films (see Supplementary Fig. 2, YAlO₃ shown in Ref.³¹), demonstrating that the amorphous phase of both the LaAlO₃ and YAlO₃ thin films is deposited on the KTaO₃(111) substrates. These results are in good agreement with that of previous studies^{23,24,31,35}. Electrical transport measurements are then performed on the as-grown thin films patterned Hall bar configurations^{31,36}.

The longitudinal electrical resistances R_s in Fig. 1a shows metallic behavior from room temperature to 2.5 K for both the heterostructures LaAlO₃/KTaO₃(111) and YAlO₃/KTaO₃(111), indicating that two-dimensional electron gases are formed at their heterointerfaces since their bulk individuals are nonmagnetic insulators. In addition, the charge carriers in both cases are electrons

with an estimated charge carrier density of $7.28 \times 10^{13} \text{ cm}^{-2}$ and $1.45 \times 10^{14} \text{ cm}^{-2}$, respectively. Notably, the superconducting transitions start at $T_c^{\text{onset}} = 2.32$ K and 2.39 K, and resistances drop to zero at $T_c^{\text{zero}} = 1.66$ K and 1.7 K, respectively, for LaAlO₃/KTaO₃ and YAlO₃/KTaO₃. At the superconducting heterointerface of LaAlO₃/KTaO₃(111), the field-dependent resistance shown in Supplementary Fig. 3 yields the upper critical fields $\mu_0 H_{c2}^\parallel(0.6 \text{ K}) = 5$ T for fields parallel to the sample plane surface and $\mu_0 H_{c2}^\perp(0.6 \text{ K}) = 0.45$ T for fields parallel to the crystallographic c -axis. Here, $\mu_0 H_{c2}$ is defined as the magnetic field at the midpoint of the electrical resistance transition. The extracted temperature dependence of the upper critical fields $\mu_0 H_{c2}$ is shown in Supplementary Fig. 3c, where a large ratio $H_{c2}^\parallel/H_{c2}^\perp$ is perceived, suggestive of strong anisotropic superconductivity of LaAlO₃/KTaO₃(111). Quantitatively, the out-of-plane polar angular θ -dependent upper critical field $\mu_0 H_{c2}^\theta$ at 1.6 K is used to further verify this intriguing behavior, as shown in Fig. 1b. Using the two-dimensional Tinkham and the three-dimensional anisotropic Ginzburg-Landau models to fit the $\mu_0 H_{c2}^\theta$, given by $\frac{H_{c2}^\theta |\cos \theta|}{H_{c2}^\perp} + \left(\frac{H_{c2}^\theta \sin \theta}{H_{c2}^\parallel}\right)^2 = 1$ and $\left(\frac{H_{c2}^\theta \cos \theta}{H_{c2}^\perp}\right)^2 + \left(\frac{H_{c2}^\theta \sin \theta}{H_{c2}^\parallel}\right)^2 = 1$, respectively^{37,38}, a cusp-like peak is clearly observed at around $\theta = 90^\circ$ (see Fig. 1b, inset), which is well described by the two-dimensional Tinkham model, as frequently observed in heterointerface superconductivity^{31,38,39} and layered transition metal dichalcogenides^{32,40}. Qualitatively similar results have also been observed in YAlO₃/KTaO₃³¹, unambiguously demonstrating the intrinsic two-dimensional superconductivity at the KTaO₃ heterointerfaces.

To further examine the intrinsic interfacial superconductivity at the KTaO₃ heterointerfaces, we also measure the current-voltage (I - V) characteristics at various temperatures close to T_c (see Supplementary Fig.

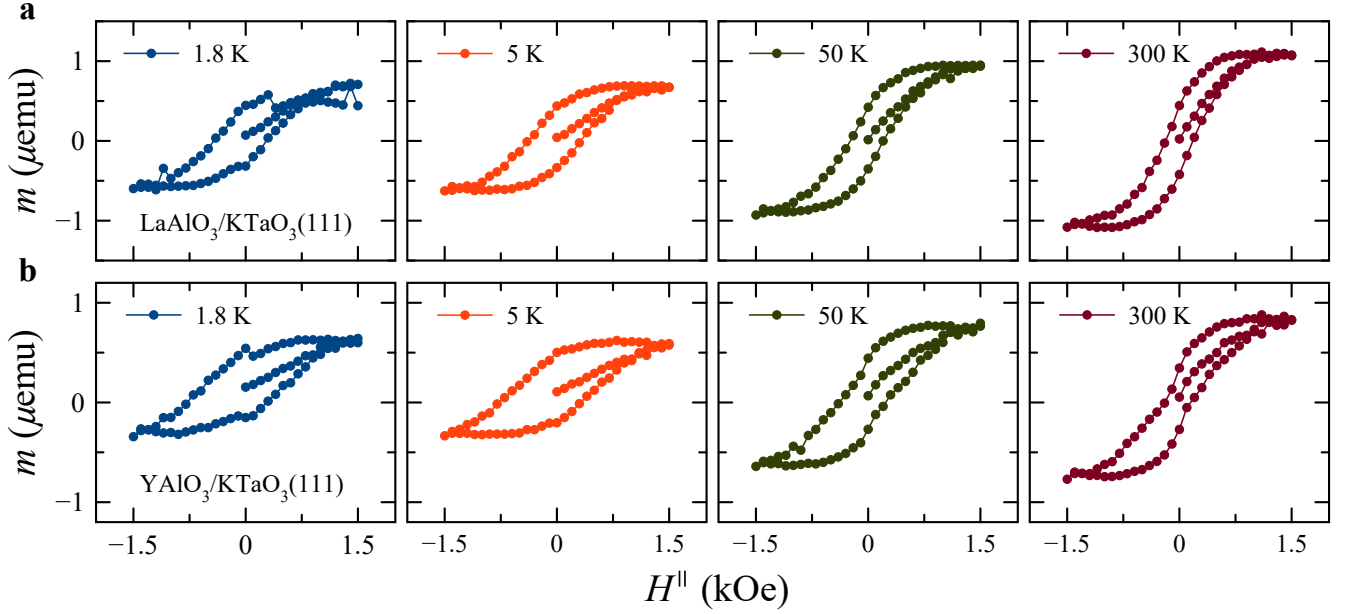


FIG. 2. **Ferromagnetic properties of KTaO₃ heterointerfaces.** Temperature-dependent in-plane m - H^{\parallel} ferromagnetic hysteresis loops of **a** LaAlO₃/KTaO₃(111) and **b** YAlO₃/KTaO₃(111) after the subtraction of the diamagnetic contribution of the bare KTaO₃ substrate at different temperatures. A magnetic field H^{\parallel} is applied parallel to the surface of thin films ranging from -1.5 kOe to +1.5 kOe.

4). They are shown using a log-log scale in Fig. 1c. Below T_c , we find a clear critical current I_c of 79.1 μ A at a temperature of 1.4 K. By increasing temperature, the value of the critical current I_c gradually decreases and then vanishes, signaling a transition from superconducting to metallic states. In the normal state, we have $V \propto I$ that is Ohm's law. As temperature drops, a steeper power law $V \propto I^{\alpha(T)}$ appears. According to the Berezinskii-Kosterlitz-Thouless (BKT) definition^{41,42}, the transition temperature T_{BKT} corresponds to the dissociation of vortex-antivortex pairs. This obeys the universal scaling relation $V \propto I^3$, since the superconducting phase consists of bound vortex-antivortex pairs in two-dimensional superconductors. We thus determine $T_{\text{BKT}} = 1.793$ K from where $\alpha = 3$ interpolates. Besides, T_{BKT} can be alternatively evaluated from the formula $R_s = R_0 \exp[-b(T/T_{\text{BKT}} - 1)^{-1/2}]$, where R_0 and b are material parameters⁴³. Application of such theoretical fit to the measured R_s yields $T_{\text{BKT}} = 1.878$ K (see Supplementary Fig. 5). As expected, the T_{BKT} obtained from these two independent approaches appears to be close to T_c^{zero} , providing an additional evidence for the two-dimensional superconducting nature of the KTaO₃ heterointerfaces.

Next, we turn to discuss the magnetic properties of KTaO₃ heterointerfaces. The two-dimensional conducting electron gases formed at the interface of KTaO₃ heterostructures are primarily formed by the partially filled 5d orbitals of the Ta atoms induced by oxygen vacancies, which themselves could lead to ferromagnetism (see also the first-principles calculations in discussion section in details). Experimentally, the zero-field-cooling (ZFC)

and field-cooling (FC) curves of the as-grown thin films of LaAlO₃ and YAlO₃ measured at temperature between 1.8 and 300 K with an applied in-plane field (H^{\parallel}) of 50 Oe are summarized in Supplementary Fig. 6. Remarkably, the figures exhibit that the separation between the ZFC and the FC curves obtained for the same magnetic field value occurs up to 300 K, showing a signature of the existence of an in-plane ferromagnetism at the superconducting KTaO₃ heterointerfaces that persists to room temperature. In Fig. 2, the well-defined magnetization-magnetic field ($m \sim H^{\parallel}$) hysteresis loops observed at different temperatures for the heterostructures LaAlO₃/KTaO₃ and YAlO₃/KTaO₃, show clear evidence for the temperature dependence of long-range ferromagnetic order. Control experiments on an as-received KTaO₃ substrate without LaAlO₃ or YAlO₃ overlayers only show a diamagnetic background (see Supplementary Fig. 7 and Supplementary Fig. 8). In addition, both the x-ray photoelectron spectroscopy (XPS) and scanning electron microscopy (SEM)-energy dispersive x-ray spectroscopy (EDS) measurements are also performed to further rule out any extrinsic magnetic contamination issue during sample preparation. As expected, no evidence of any magnetic element, such as Fe, Co, Mn, Ni or Cr, is seen in the samples (see Supplementary Fig. 9 and Supplementary Fig. 10). Consequently, the universally and consistently observed conspicuous ferromagnetic signal shown in Fig. 2 is assigned to the intrinsic nature of the KTaO₃ heterointerfaces. Namely, the appearance of the interfacial ferromagnetism is thus attributed to the Ta⁴⁺ : 5d¹ electrons that are induced by the high concentration of oxygen vacancies at the KTaO₃ heterointer-

faces²⁴ (see also the discussion section in details). This is a prominent observation considering that their bulk individuals are typical nonmagnetic insulators, which is also essentially different from previous report that the ferromagnetic response is thought to be derived from magnetic thin film of EuO ⁴⁴.

Furthermore, comparative in-plane and out-of-plane $m \sim H$ loop SQUID measurements of the $\text{LaAlO}_3/\text{KTaO}_3$ and $\text{YAlO}_3/\text{KTaO}_3$ heterostructures (Supplementary Fig. 11 - Supplementary Fig. 14) indicate that the temperature dependence of long-range ferromagnetic order lies in-plane of the KTaO_3 heterointerfaces, which is consistent with the first-principles calculations (see the discussion section in details). We also evaluate the in-plane magnetization of the itinerant electron gases formed at the KTaO_3 heterointerfaces with magnitude corresponding to $\simeq 0.2 \mu_B$ per interface unit cell (if all the magnetization is assigned to the interface). It is interesting to point out that the KTaO_3 heterointerfaces exhibit a non-monotonic behavior in temperature-dependent magnetization (see Fig. 2 and Supplementary Fig. 15). This non-monotonic behavior has also been observed in previously studied $\text{LaAlO}_3/\text{SrTiO}_3$ ¹² and VSe_2 monolayers on van der Waals substrates⁴⁵, and is ascribed to the structural phase and charge-density-wave transitions, respectively. Since KTaO_3 shares a number of properties in common with SrTiO_3 ³¹, the observed non-monotonic temperature-dependent magnetization in KTaO_3 heterointerfaces may be also attributed to the structural phase transitions. This non-monotonicity also indicates that the surface of the KTaO_3 and its phase transitions are critical for the origin of these emergent magnetic properties and that the role of YAlO_3 or LaAlO_3 overlayers is to significantly amplify these effects via the formation of the two-dimensional electron gases formed at the KTaO_3 heterointerfaces¹². Further experimental efforts would be needed to confirm this underlying nature of the observed non-monotonicity in temperature-dependent magnetization. Moreover, at the lowest temperature of this measurement limited $T = 1.8 \text{ K}$, which is also lower than T_c^{onset} [2.32 K for $\text{LaAlO}_3/\text{KTaO}_3(111)$ and 2.39 K for $\text{YAlO}_3/\text{KTaO}_3(111)$], the conspicuous signal of in-plane ferromagnetic hysteresis loops is reproducibly observed in the superconducting transition regime (see Fig. 2), and the magnetization does not seem to be completely expelled below T_c . These universal and striking results are strong reminiscent of the intrinsic spatial coexistence of superconductivity and long-range ferromagnetic order at the KTaO_3 heterointerfaces⁴⁶. Therefore, we experimentally provide a signature of the coexistence of ferromagnetism and superconductivity in the KTaO_3 heterointerface superconductors, which has also long been a topic of interest sought in condensed matter physics and material science⁴⁷.

Discussion

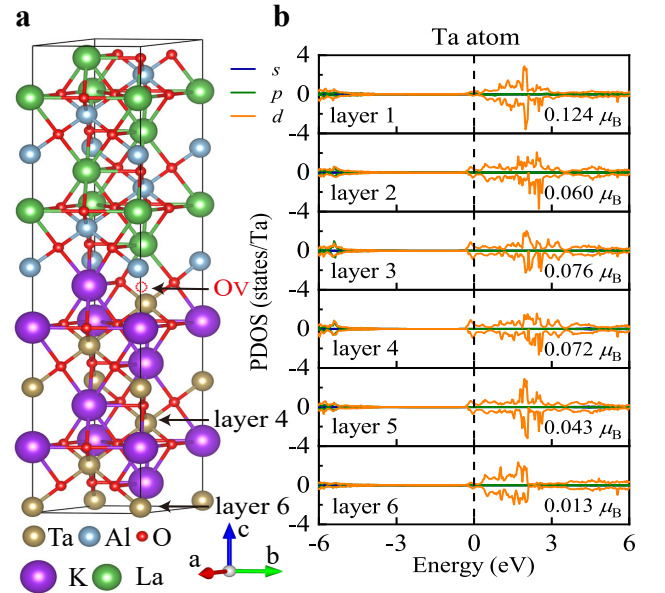


FIG. 3. First-principles calculations on the KTaO_3 heterointerface. **a** Schematic structure of the superlattices $(\text{LaAlO}_3)_6/(\text{KTaO}_3)_6(111)$ with the presence of an oxygen vacancy. The red dotted circle denotes the oxygen vacancy (Ov) at the heterointerface of $\text{LaAlO}_3/\text{KTaO}_3(111)$. **b** The PDOS for Ta atoms, calculated by using GGA+ U_{eff} method with $U_{\text{eff}} = 1.0 \text{ eV}$. The numbers listed in the figure represent the magnetization of Ta in each layer. Here, the Fermi energy is set to zero.

To gain further insight into the emergent intrinsic ferromagnetism at the KTaO_3 heterointerfaces, we proceed to discuss the underlying electronic and magnetic properties based on the first-principles calculations^{48–50}. For simplicity, we construct a theoretical model with the superlattice $(\text{KTaO}_3)_6/(\text{LaAlO}_3)_6(111)$ containing the supercell of six layers of both the LaAlO_3 and KTaO_3 ⁵¹, albeit the amorphous phase of LaAlO_3 thin films grown on the $\text{KTaO}_3(111)$ substrates (see Supplementary Fig. 2), as schematically illustrated in Fig. 3a and Supplementary Fig. 16a (see also Methods). In the stoichiometric heterostructure $(\text{KTaO}_3)_6/(\text{LaAlO}_3)_6(111)$ that is in the absence of oxygen vacancy, the calculated layer-dependent projected density-of-states (PDOS) reveal that the system is a nonmagnetic band insulator with an energy band gap of $\simeq 3.0 \text{ eV}$ (see Supplementary Fig. 16), in good agreement with previous study⁵². Furthermore, this result also indicates that the diverging Coulomb field due to the polarity of the individual layers of LaAlO_3 and KTaO_3 is unlikely to be the source of the emergent two-dimension electron gases formed at the KTaO_3 heterointerfaces, due instead to the existence of oxygen vacancies.

Principally, each oxygen vacancy donates two electrons into the $\text{LaAlO}_3/\text{KTaO}_3(111)$ interface. In turn, the induced interface charges are typically spread over adjacent layers, giving rise to a $\text{Ta}^{4+} \sim \text{O}^{2-} \sim \text{Ta}^{5+}$ -like electronic configuration, which corresponds to several partially filled Ta 5d sub-bands that can lead to interfacial

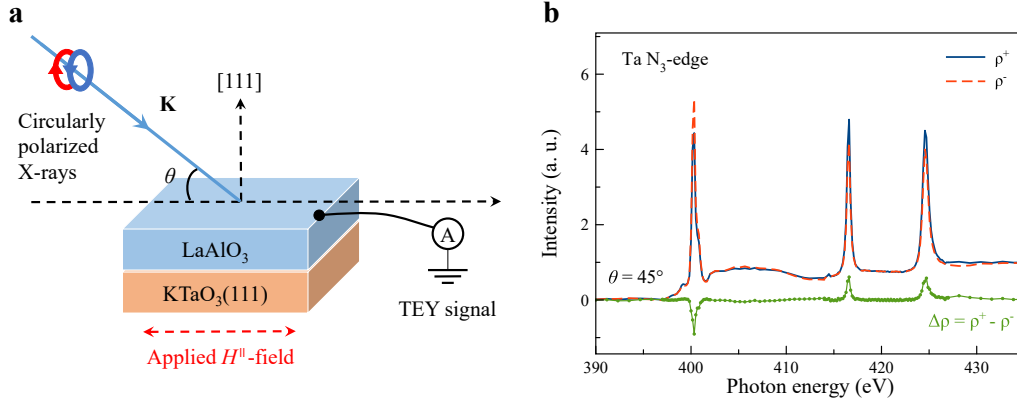


FIG. 4. **XMCD measurement on a $\text{LaAlO}_3/\text{KTaO}_3(111)$.** **a** Schematic illustration of the experimental configuration for the XMCD measurement. Here, \mathbf{K} is the x-ray propagation vector. **b** Spectrum of the XMCD at Ta N_3 absorption edge observed for the in-plane geometry with a fixed incidence angle $\theta = 45^\circ$, showing ferromagnetic Ta at $T = 15$ K. The sample is zero-field cooled and measured in a constant applied in-plane field of $H^\parallel = \pm 0.2$ T.

ferromagnetism. As expected, density functional theory calculations show that in the presence of oxygen vacancies (O_V , denoted by red dotted circle shown in Fig. 3a), the system behaves as a metal with the conducting electrons mainly derived from the Ta $5d$ orbitals partially hybridized with the oxygen $2p$ orbitals (see Supplementary Fig. 17). Furthermore, Fig. 3b shows the spin-resolved PDOS for Ta atoms associated with the value of the magnetic moments of each Ta layer. The calculated magnetic moment of Ta, brought about by the nearby oxygen vacancy, is about $0.124 \mu_B$, indicating that the long-range ferromagnetic order is an intrinsic property of the KTaO_3 heterointerface. These results are in qualitative and quantitative agreement with the magnetization measurements shown in Fig. 2. Moreover, we remark that the electron correlation effect of Ta $5d$ orbitals has been corrected via the simplified on-site repulsion strength U_{eff} on Ta $5d$ orbitals⁵³, which leads to a magnetic moment that is fairly consistent with the experimental findings shown in Fig. 3b (see also Supplementary Fig. 18 and Supplementary Fig. 19).

Experimentally, the synchrotron XMCD measurement (see Methods), owing to the element-specific technique as well as the very high sensitivity, is independently carried out to further examine whether the aforementioned interfacial ferromagnetism arises from intrinsic spin polarization of the Ta $5d$ electrons at the KTaO_3 heterointerfaces. In Fig. 4, we show the XMCD spectra of a representative $\text{LaAlO}_3/\text{KTaO}_3(111)$ near Ta N_3 absorption edge taken at a temperature $T = 15$ K under an in-plane magnetic field. Remarkably, the reproducible dichroism features appeared only near the absorption peaks (see Fig. 4b) are discernable, which are similar to those XMCD signals observed at $\text{LaAlO}_3/\text{SrTiO}_3$ heterointerfaces⁵⁴, indicating that these XMCD signals are indeed originating from intrinsic spin polarization of the Ta $5d$ electrons.

As a further control, we carry out the additional experiments that the $\text{LaAlO}_3/\text{KTaO}_3(111)$ heterostructures are re-prepared and post-annealed at various oxygen par-

tial pressures (P_{O_2}) to effectively tune the oxygen vacancies to further support the aforementioned theoretical scenario of the emergent ferromagnetism induced by oxygen vacancies, as shown in Fig. 5. As expected from our intuitions, with the increase of post-annealing P_{O_2} , the part of oxygen vacancies located at the KTaO_3 heterointerfaces will be gradually filled, resulting in the enhancement of the sheet resistance R_s (see Fig. 5a) of the two-dimensional electron gases accompanied by the substantial diminution of both the charge carrier density (see Fig. 5b) and the ferromagnetization (see Fig. 5c, d). In particular, the magnetic response for the $\text{LaAlO}_3/\text{KTaO}_3$ post-annealed at a P_{O_2} of 1 mbar is much smaller, with an almost vanishing magnetic hysteresis loop (see Fig. 5d), underscoring the pivotal role of oxygen vacancies in the emergence of interfacial ferromagnetism. These independent and complementary electrical transport and magnetization results provide the strong compelling indication for the prior conclusion that the ferromagnetic Ta at the superconducting KTaO_3 heterointerfaces is associated with the partially filled $5d$ electrons brought about by the oxygen vacancies.

Since ferromagnetism and superconductivity are generally considered to be antagonistic states of matter, an intriguing observation in Fig. 2 is the two-dimensional superconductivity experimentally found inside a ferromagnetic phase at the KTaO_3 heterointerfaces, implying that the ferromagnetic spin fluctuations probably play a crucial role in mediating the superconducting Cooper pairs⁴⁷. Importantly, the mixed-parity superconductivity with an admixture of s -wave and p -wave pairings, which is compatible with the ferromagnetism, has also been revealed at the KTaO_3 heterointerfaces³¹. In addition, it is interesting to point out that the KTaO_3 heterointerfaces behave the highest T_c of superconductivity for the ferromagnetic EuO overlayer^{23,28}, which seems that the existence of ferromagnetic spin fluctuations may reinforce superconductivity. These complementary results support a signature of the coexistence of the ferromag-

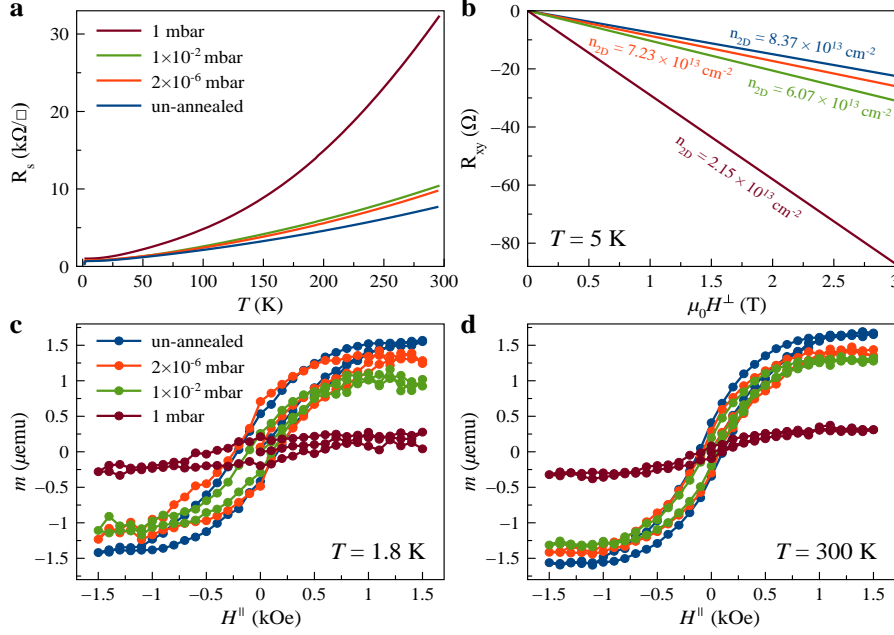


FIG. 5. **Influence of the post-annealing processes.** **a** Longitudinal electrical resistance R_s as a function of temperature for $\text{LaAlO}_3/\text{KTaO}_3(111)$ prepared under the processes of post-annealing in various oxygen partial pressures of 1, 1×10^{-2} , and 2×10^{-6} mbar. The measured data from the un-annealed sample of $\text{LaAlO}_3/\text{KTaO}_3(111)$ is also presented. **b** Corresponding perpendicular field ($\mu_0 H^\perp$)-dependent transverse Hall resistance R_{xy} measured at the temperature of 5 K. In-plane magnetic field-dependent magnetization measured at **c** 1.8 K and **d** 300 K for the films with post-annealing processes. Here, it should be noted that the diamagnetic background from the KTaO_3 substrate has been subtracted from the high field slope at each temperature measured.

netism and superconductivity at the KTaO_3 heterointerfaces. As a consequence, the superconductivity at the KTaO_3 heterointerfaces is likely to be of unconventional nature with time-reversal symmetry breaking⁵⁵, which will be exploited for quantum computing^{56–59}. Further experiments, including a local probe of the temperature dependence of the local susceptibility in the superconducting phase, such as nuclear magnetic resonance, μ -spin relaxation, and magneto-optic Kerr effect, will be helpful for elucidating the intrinsic coexistence of superconductivity and ferromagnetism at the KTaO_3 heterointerfaces that we observe.

In summary, we have experimentally grown two-dimensional superconducting heterointerfaces of KTaO_3 and observed striking in-plane ferromagnetic hysteresis loops at the verge of superconductivity that persists to above room temperature. In addition, we have also performed both the first-principles calculations and the XMCD measurements to further elucidate the intrinsic ferromagnetism emergent at the heterointerfaces of the KTaO_3 . These intriguing findings indicate KTaO_3 heterointerfaces as an unconventional superconductivity with time-reversal symmetry breaking. Our results therefore pave the way to further experimental and theoretical studies aimed at unveiling the delicate interplay among strong spin-orbit coupling, ferromagnetism, and superconductivity at the newly discovered KTaO_3 heterointerfaces.

Methods

Thin film growth and structural characterizations. RAlO_3 ($R = \text{Y, La}$) thin films are grown on $\text{KTaO}_3(111)$ substrates ($5 \times 5 \times 0.5 \text{ mm}^3$) by PLD in an ultrahigh vacuum chamber (base pressure of 10^{-9} Torr). Prior to growth, the $\text{KTaO}_3(111)$ substrates are annealed at 600°C for 30 mins in ultrahigh-vacuum to obtain a smooth surface (Supplementary Fig. 1). During deposition, single crystal YAlO_3 and LaAlO_3 targets (Kurt J. Lesker Company) are used to grow the RAlO_3 ($R = \text{Y, La}$) thin films with a KrF excimer laser (Coherent 102, wavelength: $\lambda = 248 \text{ nm}$). A pulse energy density of 1.5 J/cm^2 and a repetition rate of 2 Hz are used. The thin films are deposited at temperatures ranging from 600 to 900°C in a vacuum chamber to promote growth of the superconducting phase. All the samples are cooled to room temperature at a constant rate of 20°C/min in vacuum after deposition. The quality of thin films under ambient conditions is examined by XRD using the four-circle XRD (Bruker D8 Discover, $\text{Cu K}\alpha$ radiation, $\lambda = 1.5406 \text{ \AA}$) operated in high-resolution mode using a three-bounce symmetric Ge (022) crystal monochromator. The AFM (Asylum Research MFP-3D Classic) is used to observe the surface morphology of $\text{KTaO}_3(111)$ substrates and RAlO_3 ($R = \text{Y, La}$) thin films, and the thickness of the thin films is measured on the same footing. Furthermore, the electronic states and the chemical

compositions of the as-grown thin films are analyzed by using XPS on a Thermo Scientific system (ESCALAB QXi, XPS) with a monochromatic Al K α x-ray source (1486.6 eV) and by using SEM on a Thermo Scientific system (Quattro, SEM) with UltraDry SDD EDS detector.

Magnetization and electrical transport measurements. The magnetic properties of the $R\text{AlO}_3$ ($R = \text{Y}, \text{La}$) films are measured by using a SQUID magnetometer (MPMS3, Quantum Design Inc.). For a measurement of the direct current magnetizations as a function of temperature, the samples are first cooled in zero-field down to the lowest temperature (1.8 K), and then an in-plane magnetic field of 50 Oe is applied. The magnetization data are collected during warming from 1.8 to 300 K (ZFC process). In the same fixed field, the samples are then cooled to 1.8 K again, and the magnetization data are recollected during warming from 1.8 to 300 K (FC process). Furthermore, the Hall bar configuration is fabricated by ion-beam etching to measure the electrical transport properties. The electrical transport measurements are performed using a cryostat with temperature ranging from 1.5 to 300 K (Oxford Instruments TeslatronPT cryostat system) and a physical properties measurement system with dilution refrigerator (DR) system with temperature ranging from 50 mK to 4 K (PPMS with DR, Quantum Design).

XMCD measurements. The synchrotron XMCD measurement at the Ta N $_3$ absorption edge on a representative $\text{LaAlO}_3/\text{KTaO}_3(111)$ is performed at beam line BL07U of Shanghai Synchrotron Radiation Facility (SSRF). The spectra of XMCD is obtained by total electron yield (TEY) detection under a temperature (15 K) and an in-plane magnetic field ($H^{\parallel} = \pm 0.2$ T) with a fixed incidence angle $\theta = 45^\circ$ (see Fig. 4). The ρ^+ and ρ^- represent, respectively, the spectra with the paral-

lel and anti-parallel alignment of the magnetization direction with the photon helicity vector. The dichroism ($\Delta\rho = \rho^+ - \rho^-$) is the difference between the two spectra. We thus obtain the $\Delta\rho$ spectra by reversing the polarity (right- or left-circular) of the incident photon beam, and by changing the direction of the external magnetic field. The degree of circular polarization is above 95%.

First-principles calculations. The electronic and magnetic properties of $\text{LaAlO}_3/\text{KTaO}_3(111)$ are theoretically calculated by using the projected augmented wave formalism based on the framework of density functional theory⁶⁰, as implemented in the Vienna Ab initio Simulation Package (VASP)⁶¹. To depict the exchange and correlation functional, the generalized gradient approximation (GGA) of Perdew-Burke-Ernzerhof (PBE) functional is employed during the theoretical simulations⁶². Considering the strong electron correlation effects of the Ta 5d orbitals, the simplified GGA + U_{eff} method⁶³ is also adopted on the Ta 5d orbitals by setting the values of an effective Coulomb interaction U_{eff} . The cutoff energy for plane-wave expansion is 500 eV, and the convergence criterion for the total energy is set to be 10^{-6} eV. Before proceeding with optimization, the lattice constant of KTaO_3 is fixed to 4.04 Å and the lattice of the simplified cubic LaAlO_3 is strained to the $\text{KTaO}_3(111)$ substrate. All internal positions of the atoms are allowed to relax until the Hellmann-Feynman forces are smaller than 0.01 eV/Å. The Brillouin zone is meshed by the $9 \times 9 \times 1$ Gamma central Monkhorst-Pack grids for the superlattice $(\text{KTaO}_3)_6/(\text{LaAlO}_3)_6(111)$ containing the supercell of six layers of both the LaAlO_3 and KTaO_3 .

Data availability

The relevant data supporting our key findings are available within the article and the Supplementary Information file. All raw data generated during our current study are available from the corresponding authors upon reasonable request.

* qiaoshan@mail.sim.ac.cn

† mugang@mail.sim.ac.cn

‡ yanchen99@fudan.edu.cn

§ w.li@fudan.edu.cn

¹ Mannhart, J. & Schlom, D. G. Oxide interfaces—An opportunity for electronics. *Science* **327**, 1607-1611 (2010).

² Zubko, P. et al. Interface physics in complex oxide heterostructures. *Annu. Rev. Condens. Matter Phys.* **2**, 141-165 (2011).

³ Hwang, H. Y. et al. Emergent phenomena at oxide interfaces. *Nat. Mater.* **11**, 103-113 (2012).

⁴ Huijben, M. et al. Structure-property relation of $\text{SrTiO}_3/\text{LaAlO}_3$ interfaces. *Adv. Mater.* **21**, 1665-1677 (2009).

⁵ Ohtomo, A. & Hwang, H. Y. A high-mobility electron gas at the $\text{LaAlO}_3/\text{SrTiO}_3$ heterointerface. *Nature* **427**, 423-426 (2004).

⁶ Shalom, M. B. et al. Tuning spin-orbit coupling and superconductivity at the $\text{SrTiO}_3/\text{LaAlO}_3$ interface: A magnetotransport study. *Phys. Rev. Lett.* **104**, 126802 (2010).

⁷ Caviglia, A. D. et al. Tunable Rashba Spin-Orbit Interaction at Oxide Interfaces. *Phys. Rev. Lett.* **104**, 126803 (2010).

⁸ Soumyanarayanan, A., Reyren, N., Fert, A., & Panagopoulos, C. Emergent phenomena induced by spin-orbit coupling at surfaces and interfaces. *Nature* **539**, 509-517 (2016).

⁹ Reyren, N. et al. Superconducting interfaces between insulating oxides. *Science* **317**, 1196-1199 (2007).

¹⁰ Caviglia, A. D. et al. Electric field control of the $\text{LaAlO}_3/\text{SrTiO}_3$ interface ground state. *Nature* **456**, 624-627 (2008).

¹¹ Brinkman, A. et al. Magnetic effects at the interface between non-magnetic oxides. *Nat. Mater.* **6**, 493-496 (2007).

- ¹² Ariando et al. Electronic phase separation at the $\text{LaAlO}_3/\text{SrTiO}_3$ interface. *Nat. Commun.* **2**, 188 (2011).
- ¹³ Li, L., Richter, C., Mannhart, J., & Ashoori, R. C. Coexistence of magnetic order and two-dimensional superconductivity at $\text{LaAlO}_3/\text{SrTiO}_3$ interfaces. *Nat. Phys.* **7**, 762-766 (2011).
- ¹⁴ Bert, J. A. et al. Direct imaging of the coexistence of ferromagnetism and superconductivity at the $\text{LaAlO}_3/\text{SrTiO}_3$ interface. *Nat. Phys.* **7**, 767-771 (2011).
- ¹⁵ Dikin, D. A. et al. Coexistence of superconductivity and ferromagnetism in two dimensions. *Phys. Rev. Lett.* **107**, 056802 (2011).
- ¹⁶ Michaeli, K., Potter, A. C., & Lee, P. A. Superconducting and ferromagnetic phases in $\text{SrTiO}_3/\text{LaAlO}_3$ oxide interface structures: Possibility of finite momentum pairing. *Phys. Rev. Lett.* **108**, 117003 (2012).
- ¹⁷ Kozii, V. & Fu, L. Odd-parity superconductivity in the vicinity of inversion symmetry breaking in spin-orbit-coupled systems. *Phys. Rev. Lett.* **115**, 207002 (2015).
- ¹⁸ Han, Y.-L. et al. Two-dimensional superconductivity at (110) $\text{LaAlO}_3/\text{SrTiO}_3$ interfaces. *Appl. Phys. Lett.* **105**, 192603 (2014).
- ¹⁹ Monteiro, A. M. R. V. L. et al. Two-dimensional superconductivity at the (111) $\text{LaAlO}_3/\text{SrTiO}_3$ interface. *Phys. Rev. B* **96**, 020504(R) (2017).
- ²⁰ Fitzsimmons, M. R. et al. Upper limit to magnetism in $\text{LaAlO}_3/\text{SrTiO}_3$ heterostructures. *Phys. Rev. Lett.* **107**, 217201 (2011).
- ²¹ Salman, Z. et al. Nature of weak magnetism in $\text{SrTiO}_3/\text{LaAlO}_3$ multilayers. *Phys. Rev. Lett.* **109**, 257207 (2012).
- ²² Pai, Y.-Y., Tylan-Tyler, A., Irvin, P., & Levy, J. *Spintronics Handbook: Spin Transport and Magnetism* (CRC Press, 2019).
- ²³ Liu, C. et al. Two-dimensional superconductivity and anisotropic transport at KTaO_3 (111) interfaces. *Science* **371**, 716-721 (2021).
- ²⁴ Chen, Z. et al. Two-dimensional superconductivity at the $\text{LaAlO}_3/\text{KTaO}_3$ (110) heterointerface. *Phys. Rev. Lett.* **126**, 026802 (2021).
- ²⁵ Ueno, K. et al. Discovery of superconductivity in KTaO_3 by electrostatic carrier doping. *Nat. Nanotechnol.* **6**, 408-412 (2011).
- ²⁶ Bruno, F. Y. et al. Band structure and spin-orbital texture of the (111)- KTaO_3 2D electron gas. *Adv. Electron. Mater.* **5**, 1800860 (2019).
- ²⁷ Mallik, S. et al. Superfluid stiffness of a KTaO_3 -based two-dimensional electron gas. *Nat. Commun.* **13**, 4625 (2022).
- ²⁸ Hua, X. et al. Tunable two-dimensional superconductivity and spin-orbit coupling at the EuO/KTaO_3 (110) interface. *npj Quantum Mater.* **7**, 97 (2022).
- ²⁹ Arnault, E. G. et al. Anisotropic superconductivity at KTaO_3 (111) interfaces. *Sci. Adv.* **9**, eadf1414 (2023).
- ³⁰ Krantz, P., Tyner, A., Goswami, P., & Chandrasekhar, V. Colossal spontaneous Hall effect and emergent magnetism in KTaO_3 two-dimensional electron gases. arXiv:2209.10534 (2022).
- ³¹ Zhang, G. et al. Spontaneous rotational symmetry breaking in KTaO_3 interface superconductor. *Nat. Commun.* **14**, 3046 (2023).
- ³² Jiang, D. et al. Strong in-plane magnetic field induced reemergent superconductivity in the van der Waals heterointerface of NbSe_2 and CrCl_3 . *ACS Appl. Mater. Interfaces* **12**, 49252-49257 (2020).
- ³³ Zou, M. et al. Evidence for ferromagnetic order in the CoSb layer of LaCoSb_2 . *Phys. Rev. B* **101**, 155138 (2020).
- ³⁴ Yuan, T.-Z. et al. Pairing symmetry in monolayer of orthorhombic CoSb. *Front. Phys.* **16**, 43500 (2021).
- ³⁵ Chen, Z. et al. Electric field control of superconductivity at the $\text{LaAlO}_3/\text{KTaO}_3$ (111) interface. *Science* **372**, 721-724 (2021).
- ³⁶ Xue, H. et al. Fourfold symmetric superconductivity in spinel oxide LiTi_2O_4 (001) thin films. *ACS Nano* **16**, 19464-19471 (2022).
- ³⁷ Tinkham, M. Effect of fluxoid quantization on transitions of superconducting films. *Phys. Rev.* **129**, 2413-2422 (1963).
- ³⁸ Wang, L. et al. Two-dimensional superconductivity at the titanium sesquioxide heterointerface. *ACS Nano* **16**, 16150-16157 (2022).
- ³⁹ Zhang, G. et al. Quantum metallic state in the titanium sesquioxide heterointerface superconductor. arXiv:2211.04035 (2022).
- ⁴⁰ Lu, J. M. et al. Evidence for two-dimensional Ising superconductivity in gated MoS_2 . *Science* **350**, 1353-1357 (2015).
- ⁴¹ Kosterlitz, J. M. & Thouless, D. J. Long range order and metastability in two dimensional solids and superfluids. *J. Phys.: Condens. Matter* **5**, L124-L126 (1972).
- ⁴² Beasley, M. R., Mooij, J. E., & Orlando, T. P. Possibility of vortex-antivortex pair dissociation in two-dimensional superconductors. *Phys. Rev. Lett.* **42**, 1165-1168 (1979).
- ⁴³ Halperin, B. I. & Nelson, D. R. Resistive transition in superconducting films. *J. Low Temp. Phys.* **36**, 599-616 (1979).
- ⁴⁴ Zhang, H. et al. High-mobility spin-polarized two-dimensional electron gases at EuO/KTaO_3 interfaces. *Phys. Rev. Lett.* **121**, 116803 (2018).
- ⁴⁵ Bonilla, M. et al. Strong room-temperature ferromagnetism in VSe_2 monolayers on van der Waals substrates. *Nat. Nanotechnol.* **13**, 289-293 (2018).
- ⁴⁶ Pfeleiderer, C. Superconducting phases of f -electron compounds. *Rev. Mod. Phys.* **81**, 1551-1624 (2009).
- ⁴⁷ Ghosh, S. K. et al. Recent progress on superconductors with time-reversal symmetry breaking. *J. Phys.: Condens. Matter* **33**, 033001 (2021).
- ⁴⁸ Zhou, Z. et al. Universal critical behavior in the ferromagnetic superconductor $\text{Eu}(\text{Fe}_{0.75}\text{Ru}_{0.25})_2\text{As}_2$. *Phys. Rev. B* **100**, 060406(R) (2019).
- ⁴⁹ Huang, W.-C., Li, W., & Liu, X. Exotic ferromagnetism in the two-dimensional quantum material C_3N . *Front. Phys.* **13**, 137104 (2018).
- ⁵⁰ Li, W., Zhu, J.-X., Chen, Y., & Ting, C. S. First-principles calculations of the electronic structure of iron-pnictide $\text{EuFe}_2(\text{As,P})_2$ superconductors: Evidence for antiferromagnetic spin order. *Phys. Rev. B* **86**, 155119 (2012).
- ⁵¹ Popović, Z. S., Satpathy, S., & Martin, R. M. Origin of the two-dimensional electron gas carrier density at the LaAlO_3 on SrTiO_3 interface. *Phys. Rev. Lett.* **101**, 256801 (2008).
- ⁵² Fujii, Y. & Sakudo, T. Dielectric and optical properties of KTaO_3 . *J. Phys. Soc. Jpn.* **41**, 888-893 (1976).
- ⁵³ Pentcheva, R. & Pickett, W. E. Correlation-driven charge order at the interface between a Mott and a band insulator. *Phys. Rev. Lett.* **99**, 016802 (2007).
- ⁵⁴ Lee, J.-S. et al. Titanium d_{xy} ferromagnetism at the $\text{LaAlO}_3/\text{SrTiO}_3$ interface. *Nat. Mater.* **12**, 703-706 (2013).
- ⁵⁵ Stewart, G. R. Unconventional superconductivity. *Adv. Phys.* **66**, 75-196 (2017).

- ⁵⁶ Nayak, C. et al. Non-Abelian anyons and topological quantum computation. *Rev. Mod. Phys.* **80**, 1083-1159 (2008).
- ⁵⁷ Alicea, J. New directions in the pursuit of Majorana fermions in solid state systems. *Rep. Prog. Phys.* **75**, 076501 (2012).
- ⁵⁸ Beenakker, C. W. J. Search for Majorana fermions in superconductors. *Annu. Rev. Condens. Matter Phys.* **4**, 113-136 (2013).
- ⁵⁹ Elliott, S. R. & Franz, M. Majorana fermions in nuclear, particle, and solid-state physics. *Rev. Mod. Phys.* **87**, 137-163 (2015).
- ⁶⁰ Blöchl, P. E. Projector augmented-wave method. *Phys. Rev. B* **50**, 17953-17979 (1994).
- ⁶¹ Kresse, G. & Furthmüller, J. Efficient iterative schemes for ab initio total-energy calculations using a plane-wave basis set. *Phys. Rev. B* **54**, 11169-11186 (1996).
- ⁶² Perdew, J. P., Burke, K., & Ernzerhof, M. Generalized gradient approximation made simple. *Phys. Rev. Lett.* **77**, 3865-3868 (1996).
- ⁶³ Liechtenstein, A. I., Anisimov, V. I., & Zaanen, J. Density-functional theory and strong interactions: Orbital ordering in Mott-Hubbard insulators. *Phys. Rev. B* **52**, R5467-R5470 (1995).

Acknowledgements

This work is supported by the National Natural Science Foundation of China (Grant Nos. 11927807 and U2032207) and Shanghai Science and Technology Committee (Grant Nos. 23ZR1404600 and 20DZ1100604).

The authors also thank beamline BL07U of the Shanghai Synchrotron Radiation Facility (SSRF).

Author contributions

Z.N., J.Q., and Y.L. contributed equally to this work. W.L. and Y.C. conceived the project and designed the experiments. Z.N. and G.Z. grew the samples. Z.N., Y.L., F.C., G.Z., and G.M. performed the electrical transport measurements. Z.N. and Y.L. performed the magnetization measurements. M.Z., L.D., and S.Q. performed the XMCD measurement. X.Y. and Q.G. performed the XPS measurement. X.Y., Q.G., and H.J. performed the SEM measurement. W.P. and Y.C. assisted the magnetization, electrical transport and SEM experiments. J.Q. performed the first-principles calculations. W.L. wrote the paper with input from Z.N. and J.Q.. All authors discussed the results and gave approval to the final version of the manuscript.

Competing interests

The authors declare no competing interests.

Correspondence and requests for materials should be addressed to S. Qiao, G. Mu, Y. Chen, or W. Li.

To whom correspondence should be addressed. E-mail: qiaoshan@mail.sim.ac.cn (S. Qiao), mugang@mail.sim.ac.cn (G. Mu), yanchen99@fudan.edu.cn (Y. Chen) or w.li@fudan.edu.cn (W. Li).